Electronic Supplementary Material (ESI) for Faraday Discussions.

Supporting Information

Bridging energy bands to the crystalline and amorphous states of Si QDs

Bruno Alessi[1], Manuel Macias-Montero[2], Chiranjeevi Maddi[1], Paul Maguire[1], Vladimir Svrcek[3], Davide Mariotti[1]*

[1]Nanotechnology and Integrated Bio-Engineering Centre (NIBEC), Ulster University, Newtownabbey BT37 0QB, United Kingdom

[2]Laser Processing Group, Institute of Optics (CSIC), Serrano 121, 28006 Madrid, Spain

[3]Research Center for Photovoltaics National Institute of Advanced Industrial Science and Technology (AIST) Central 2, Umezono 1–1–1, Tsukuba, 305–8568, Japan

*e-mail: alessi-b@ulster.ac.uk

S1. Reactor design

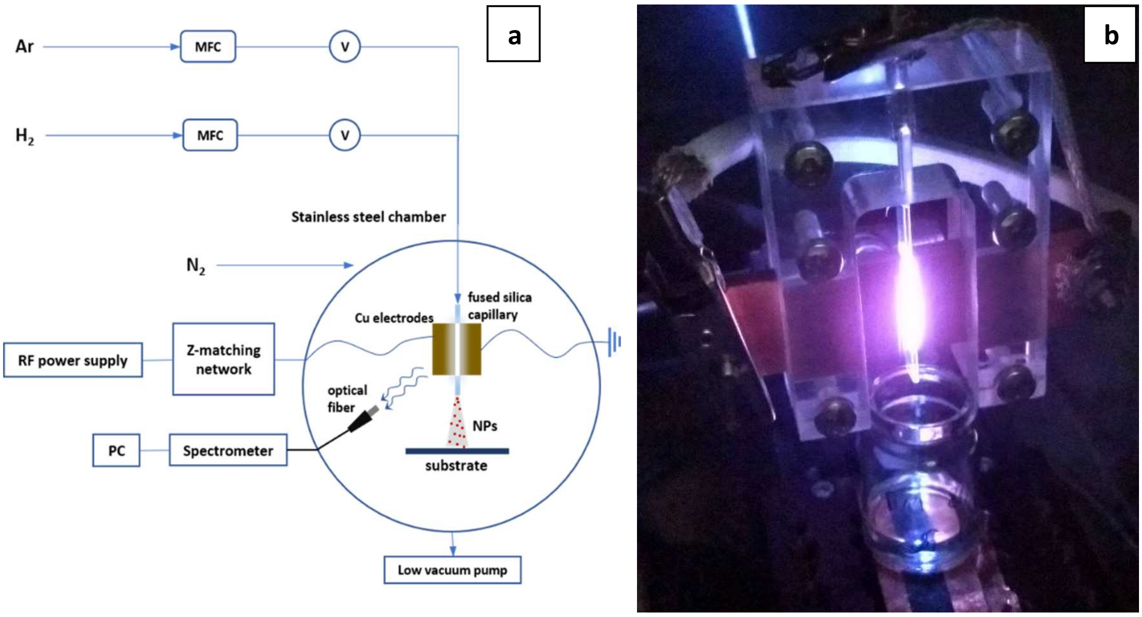

Figure S1 – **a)** Schematics of the experimental setup: gas mixing circuit, reactor chamber and setup for OES. The optical fiber is pointing perpendicularly to the capillary in the middle of the visible discharge to capture a horizontal LOS, **b)** photograph of the micro-plasma reactor operating an 80 W Ar plasma with an ethanol vial is placed directly below the capillary exit to obtain directly a colloid.

S2. Selected area electron diffraction pattern of crystalline Si quantum dots.

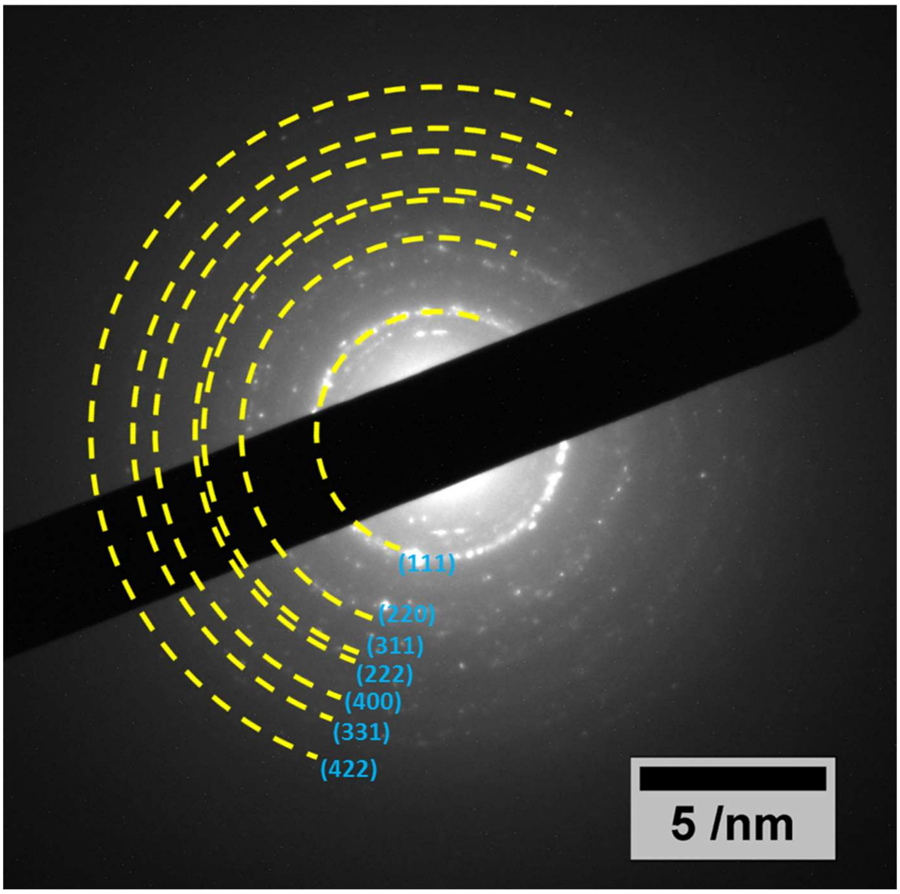

Figure S2. Selected area electron diffraction of crystalline Si quantum dots. Crystalline planes are indicated in the diffractogram.

S3. Evaluation of particle size distribution using transmission electron microscopy.

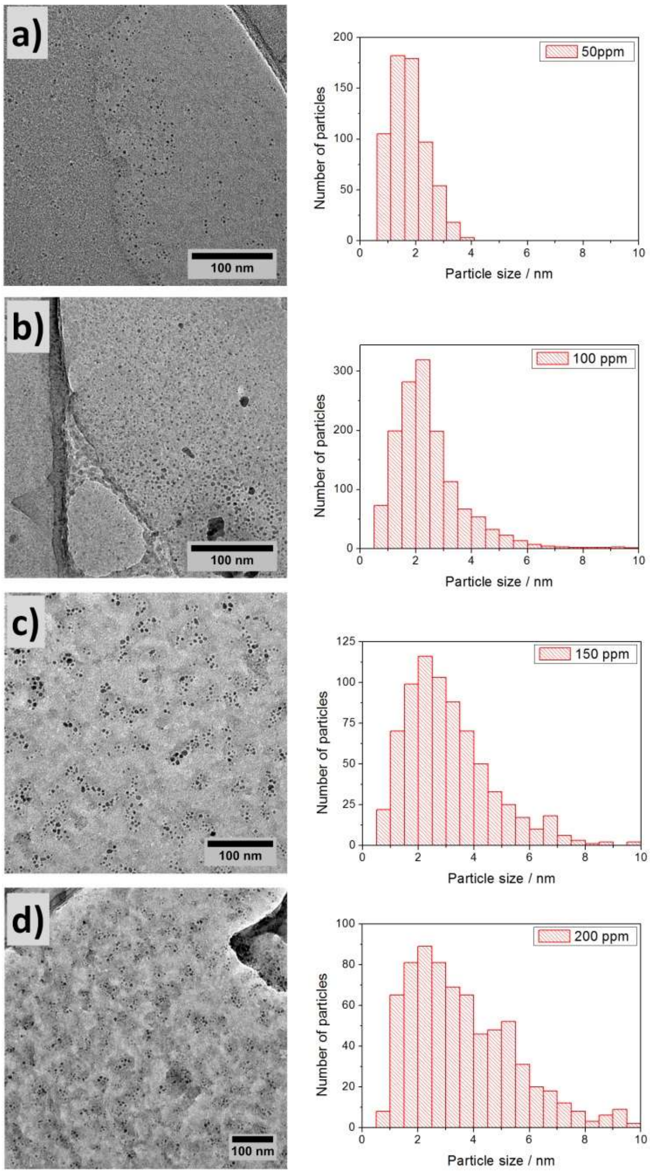

Figure S3. Transmission electron microscopy images (left panels) and particle size histogram (right panels) obtained for different precursor concentrations in the plasma: **a)** 50 ppm, **b)** 100 ppm, **c)** 150 ppm and **d)** 200ppm.

S4. REELS Spectrum

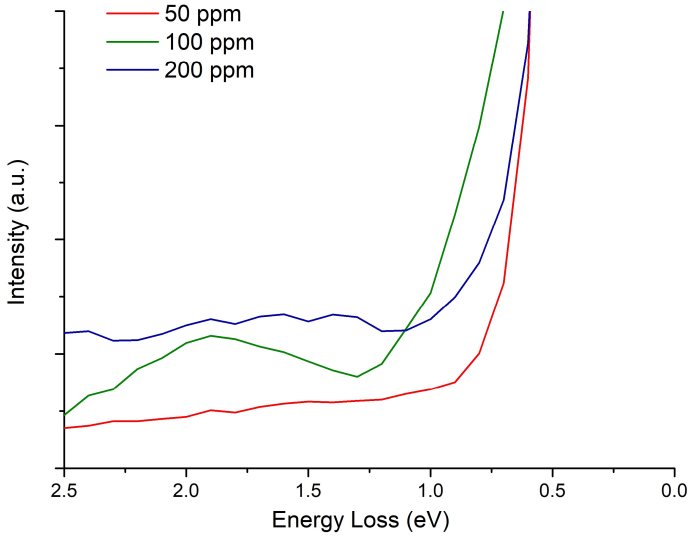

Figure S4a. REELS spectra near the Zero-loss peak (ZLP), showing (especially for 100 ppm SiH4) a feature at 1.8 eV which is usually assigned to the presence of hydrogen within the sampled volume.

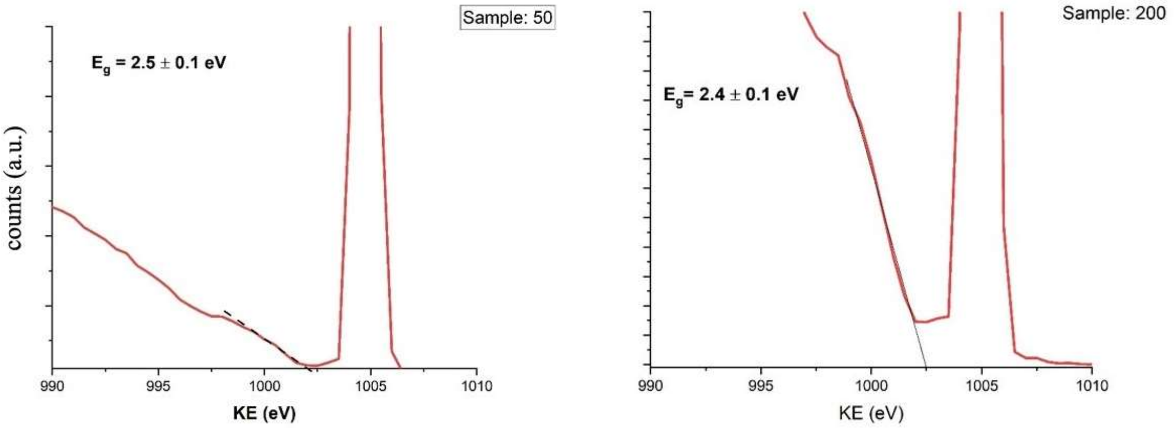

Figure S4b. Wider scan REELS spectra of 50 ppm and 200 ppm samples, showing an estimation of the electron energy Bandgap estimated from the drop in electron counts near the ZLP. Values compare very well with the optical bandgap obtained from Tauc plots. In both spectra the Zero Loss Peak is centred at 1005 eV Kinetic Energy.

S5. Calculation of the electron density from H_α emission line broadening

To fully understand the formation process of the Si QDs it is necessary to characterize the plasma parameters of the system for the different experimental conditions under study. Due to the reduced plasma size and the atmospheric pressure working conditions, it is difficult to directly use many traditional low-pressure plasma characterization techniques. However, optical emission spectroscopy (OES) remains a viable non-invasive plasma diagnostic technique. In order to develop our theoretical analysis (see further below), three important parameters have to be considered. These are gas temperature (T_g), electron temperature (T_e) and electron density (n_e), which can be estimated using OES as follows. The gas temperature can be determined from the relation of the rotational levels of OH radicals [1]. In our case, this temperature is estimated to be approximately constant for all the conditions under consideration with a value of 490 K.

The effective electron temperature is calculated using argon emission lines. In particular, Boltzmann plots for 4p and 5p levels of argon are used to calculate the excitation temperature that, in a second step, is converted to electron temperature through collisional-radiative modeling of argon lines [2]. Effective T_e decreases from 1.2 eV to 0.9 eV with increasing plasma SiH_4 concentration from 50 ppm to 150 ppm, figure S5. However, at the highest precursor concentration (200 ppm) effective T_e increases to 1.2 eV.

The electron density is determined from the Stark broadening of the Hα (λ_0 = 656.28 nm) emission line, taking into account other sources of broadening, including instrumental broadening ($\Delta\lambda_i$).

Figure S5 displays the electron density determined using the detailed procedure for the different experimental conditions under consideration. The results show that the electron density gradually decreases from $1.8 \cdot 10^{14}$ cm^{-3} to $0.8 \cdot 10^{14}$ cm^{-3} when the SiH_4 concentration is increased from 50 ppm to 200 ppm.

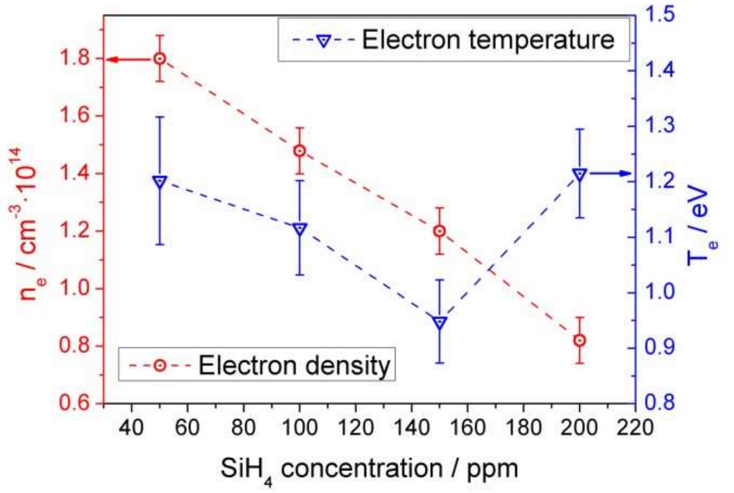

Figure S5. Electron density (left axis) and electron temperature (right axis) calculated for different silane precursor concentration introduced in the plasma.

Doppler broadening ($\Delta\lambda_D$) appears due to the thermal motion of the emitting atoms in the plasma and can be estimated as

$$\Delta\lambda_D = 7.162 \cdot 10^{-7}\lambda_0\sqrt{\frac{T_g}{M}} \qquad (1)$$

with λ_0 Hα wavelength in nm, T_g the gas temperature in K and M the atomic mass of hydrogen in atomic mass units.

As the excited atoms interact with neutral ground state atoms of other species, Van der Waals broadening ($\Delta\lambda_W$) is an important broadening mechanism in atmospheric-pressure plasmas and it can be calculated by

$$\Delta\lambda_W(cm) = 8.2 \cdot 10^{-12}\lambda_0{}^2(\alpha\langle R^2\rangle)^{2/5}\left(\frac{T_g}{M}\right)^{3/10}N \qquad (2)$$

where α is the mean atomic polarizability of the neutral perturber and N is the neutral ground-state atom density in cm^{-3}. $\langle R^2\rangle$ is the square difference of the mean coordinate vector of the radiating atom for the upper and lower levels. By considering the relationship of N with pressure P and temperature T_g, $\Delta\lambda_W$ can be simplified as $\Delta\lambda_W(nm) = 3.6 \cdot P/T_g{}^{0.7}$. Stark broadening ($\Delta\lambda_S$) is related to the electron density by the following relationship

$$\Delta\lambda_S(nm) = 4.8 \cdot \left(\frac{n_e}{10^{17}cm^{-3}}\right)^{0.68116} \qquad (3)$$

where n_e is the electron density in cm^{-3}. In order to de-convolute the experimental Hα signal ($\Delta\lambda_E$), it is necessary to consider that $\Delta\lambda_i$ and $\Delta\lambda_D$ present Gaussian profiles and $\Delta\lambda_W$ and $\Delta\lambda_S$ Lorentz profile. The combination results in a Voigt profile that can be described as:

$$\Delta\lambda_E = \left[\left(\frac{\Delta\lambda_S+\Delta\lambda_W}{2}\right)^2 + {\Delta\lambda_D}^2 + {\Delta\lambda_i}^2\right]^{1/2} + \frac{\Delta\lambda_S+\Delta\lambda_W}{2} \qquad (4)$$

[1] P. Bruggeman et al. Plasma Sources Sci. Technol. 19 (2010) 015016 (7pp)

[2] Zhu XM, Chen WC and Pu YK 2008 J. Phys. D: Appl. Phys. 41, 105212

[3] Hofmann S, van Gessel AFH, Verreycken T and Bruggeman P 2011 Plasma Sources Sci. Technol. 20, 065010

S6. Collision corrected model and heat balance on particle's surface

The plasma heating model only considers the effect of argon atoms on the heating of particles. The methodology consists of two separate steps. Firstly, the particle potential is calculated assuming it is equal to the floating potential when electron and ion fluxes are equalized, i.e., $I_e = I_i$. Secondly, the particle temperature is obtained from the balance of energy fluxes to and from the surface of a particle assuming a steady state.

Low-pressure plasmas are commonly modeled using the orbital motion limited (OML) model that provides an adequate evaluation of the electric potential of a particle immersed in the plasma. However, the OML model gives acceptable values for the floating potential only when the condition $l_i \gg \lambda_d \gg a$ is satisfied, where l_i is the ion mean free path, λ_d the plasma screening length and a is the particle radius. For APPs l_i is of the same order of λ_d, limiting the accuracy of the OML model. Hence, the effect of ion collisions and charge-exchange collisions with neutrals plays an important role. The general result is a particle's size dependence of charge accumulated on each single particle's surface that leads to an increased surface temperature in respect to base gas temperature, and the effect is stronger the smaller the particles and the bigger the difference between electron temperature and gas temperature.

The following analytical expression

$$I_i = \left[\frac{1}{I_i^{WC}} + \frac{1}{I_i^{SC}}\right]^{-1} \qquad (1)$$

describes a collision-corrected model (CCM) that considers the effect of ion-neutral collisions on the ion current. The term I_i^{WC} in equation (1) corresponds to the weakly collisional regime and can be estimated as

$$I_i^{WC} \approx \pi a^2 n_i \sqrt{\frac{8k_bT_i}{\pi M}}\left[1 - \frac{eV_p}{k_bT_i} + 0.1\left(-\frac{eV_p}{k_bT_i}\right)^2\left(\frac{\lambda_d}{l_i}\right)\right] \qquad (2)$$

where n_i is the ion density that, due to charge neutrality $n_i = n_e$, k_b is the Boltzmann constant, T_i is the ion temperature which is assumed to be equal to T_g, M is the mass of Ar ions, e is the electron charge and V_p is the floating potential. The second term in equation (1) describes the contribution of ions in a strongly collisional regime were more than one collision is expected, that is

$$I_i^{SC} = 4\pi a n_i l_i \sqrt{\frac{8k_bT_i}{\pi M}} \cdot \frac{e|V_p|}{k_bT_i} \qquad (3)$$

The electron flux to the particle surface is

$$I_e = \pi a^2 n_e \sqrt{\frac{8k_bT_e}{\pi\, m_e}} \cdot exp\left(\frac{eV_p}{k_bT_e}\right) \qquad (4)$$

where n_e is the electron density, T_e is the electron temperature and m_e is the electron mass. Therefore, the floating potential is obtained from matching equations (1) and (4) for the different n_e ant T_e measured in each of the experimental conditions presented in Figure S6.

To evaluate the particle heating mechanisms, the steady-state energy balance on the surface of the particle can be written as

$$q_{con} = q_{kin} + q_{rec} \qquad (5)$$

where q_{kin} and q_{rec} represent the rates of energy transfer via kinetic energy of charged species (ions and electrons) and ion-electron recombination on the particle surface, while q_{con} is the heat loss rate to the surrounding gas through heat conduction. Equation (5) is valid for particles smaller than 100 nm . Expressions defining the different rates are described in Table S6. Looking at the expressions at Table S6, it is possible to observe that q_{con} depends on the particle temperature (T_p). Hence, it is possible to derive an analytical expression to calculate T_p from the definition of q_{con} and equation (5).

Definition	Equation
Heat loss rate to the surrounding gas through heat conduction	$q_{con} = \frac{8\pi a^2 \mathrm{Kn}}{2a + lG}\,(T_p - T_g)$
Knudsen number Mean free path Geometry dependent heat transfer factor Eucken factor Heat capacity ratio Thermal accommodation coefficient	$\mathrm{Kn} = \frac{l}{a}$ $l = \frac{\mathrm{Kn}}{pf}\,(\gamma - 1)\sqrt{\frac{\pi M T_g}{2k_b}}$ $G = \frac{8f}{\alpha(\gamma + 1)}$ $f = \frac{9\gamma - 5}{4}$ $\gamma = \frac{C_p}{C_v}$ $\alpha = 1$ (full accommodation)
Kinetic energy transfer of charged species on the particle surface	$q_{kin} = I_i(2k_bT_e - eV_p)$
Ion-electron recombination on the particle surface	$q_{rec} = I_i\varepsilon_i$

Table S6. *Heat transfer rates and subsequent expressions along the surface of the particles immersed in the plasma region.*

The particle temperature can be written as

$$T_p = T_g + \Delta T_c \qquad (6)$$

where ΔT_c is the increment of particle temperature due to collisions inside the plasma and can be expressed as:

$$\Delta T_c = \left(\frac{2a+l}{8\pi a^2 \mathrm{Kn}}\right) I_i\,(2k_bT_e - eV_p + \varepsilon_i) \qquad (7)$$

ΔT_c is proportional to a geometric factor (first term in the equation), to the ion flux impinging the particle surface and to the energy exchange on the particle surface. At this point, it is possible to estimate T_p by introducing in equation the values of V_p and I_i obtained from equalizing equations (1) and (4).

More details can be found in:

[4] Askari S, Levchenko I, Ostrikov K, Maguire KP and Mariotti D 2014 *Appl. Phys. Lett.* **104**, 163103.

S7. Bandgap determination silicon quantum dots.

In order to evaluate the bandgap of silicon QDs it is necessary first to calculate the absorption coefficient that, in a second step, will be introduced in a Tauc plot. The following expression allows calculating the absorption coefficient

$$\alpha = -\frac{\ln(T)}{L}\,\frac{1-(T+R)}{1-T}$$

where L is the effective thickness of the Si QDs film, T is the transmittance and R accounts for specular reflectance and scattering of the sample. T and T+R were obtained using the UV-vis system described in the experimental section that includes an integrating sphere to evaluate the scattering of the materials.

To find a value for the bandgap the absorption coefficient is introduced in a Tauc plot. In this plot $(\alpha \cdot E)^d$ vs E are ploted, where E is the photon energy and d is a coefficient. Depending on the nature of the bandgap d can have different values. In our case, silicon in known to have an indirect bandgap which corresponds to d= ½. Projecting the linear part of the Tauc plot towards the x-axis provides a value for the bandgap of the material. As an example, Figure S7 displays a Tauc plot of Si QDs grown using 50 ppm and 200 ppm of silane during the synthesis process.

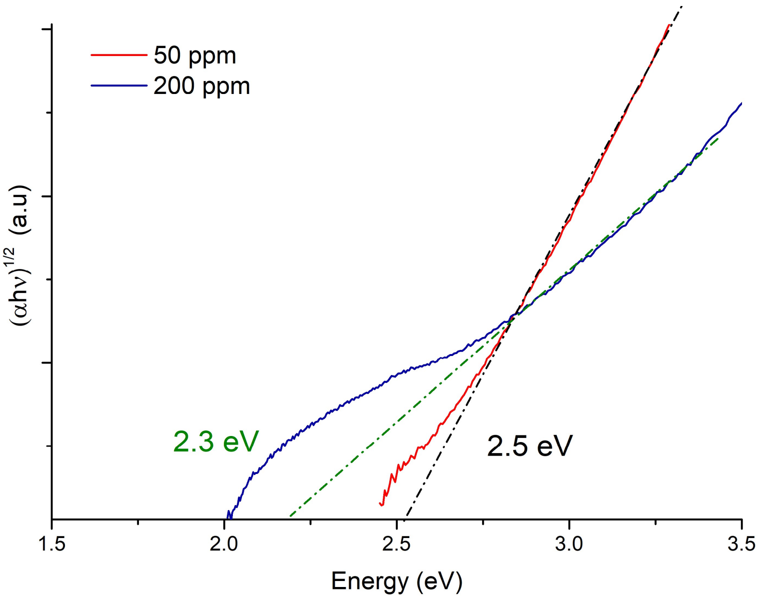

Sample	Fit Data range (meV)	R^2	Eg (eV)	ΔE (eV)
50 ppm	80	0.999	2.5	± 0.1
200 ppm	70	0.997	2.3	± 0.1

Figure S7. Tauc plots with relative best fit lines for the bandgap determination of Si QDs samples at 50 and 200 ppm of silane, which resulted respectively in all-crystalline 1.8 nm particles and all-amorphous 3.6 nm particles. The table indicates the statistical confidence of fits in terms of width of the data range chosen for the linear fit, R^2 coefficient and errors obtained.

S8. SPS Spectra for bandgap determination

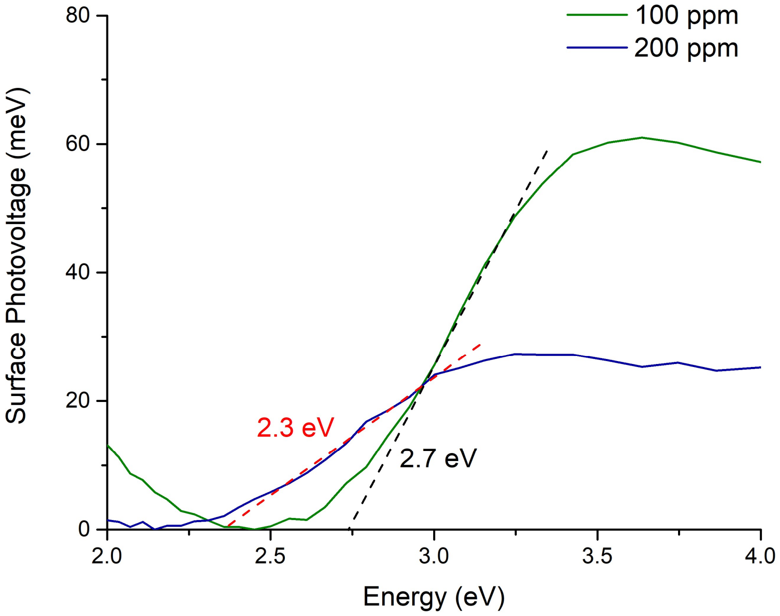

Comparison of bandgap measurements

Figure S8. SPS spectrum of two amorphous particles-containing samples, showing a good match between the energy threshold to induce a photovoltage and the relative UV-VIS energy gaps obtained with Tauc Plots

Sample	**REELS (figure S4b)**	**Absorption (figure S7)**	**SPS (figure S8)**
50 ppm	2.5 eV	2.5 eV	2.7 eV
200 ppm	2.4 eV	2.3 eV	2.3 eV

S9. APS spectra and extraction of VBM

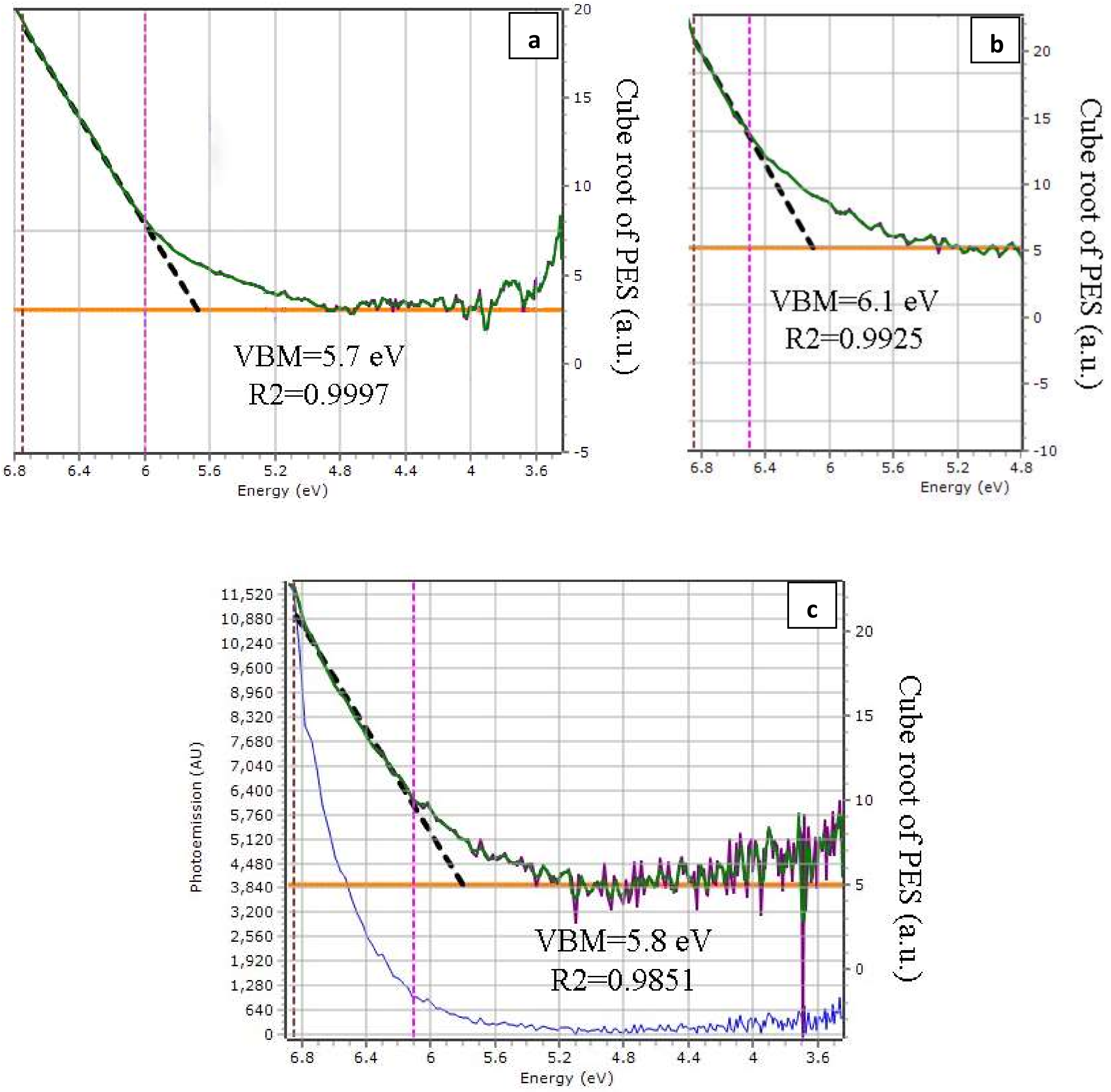

Figure S9 – Air photoemission spectra can give the values of VBM for a semiconductor [5], calculating a best-fit line of the cube root of the photoemission signal and extrapolating the intercept with the energy axis. Plots and best-fits for **a)** 50 ppm , **b)** 100 ppm and **c)** 200 ppm of SiH4.

[5] Iain D. Baikie et al. / Energy Procedia 60 (2014) 48 – 56

S10. Solar cell design based on SiQDs and CuO QDs

In a second device architecture we maintained the same structure for the bottom part of the device, i.e. the ITO/TiO_2/Si QDs structure was unchanged. However, we replaced the Cu_2O transport layer with an additional layer of surface treated p-type Si nanocrystals before depositing a CuO QDs transport layer (figure S10 in supporting information). The p-type Si nanocrystals were obtained by electrochemical etching of Si wafers; characterization and synthesis details can be found elsewhere [6,7]. The plasma-produced Si QDs film and the layer formed by p-type Si nanocrystals are expected to establish a junction, intended to increase the density of generated carriers. CuO QDs were obtained by an APP-liquid method, following the protocol previously detailed [8]. A magnetron sputtered Au film was deposited through a mask as the top contact. Unfortunately, the expected improvements did not materialize (table S10 and figures S10) and this suggests that the use of a single absorber in QDs solar cells is a better approach. The values for the shunt and series resistance are the result of the interlayer contact, which is not conformal and where a plethora of different trap states for carriers are expected to hamper their transport properties

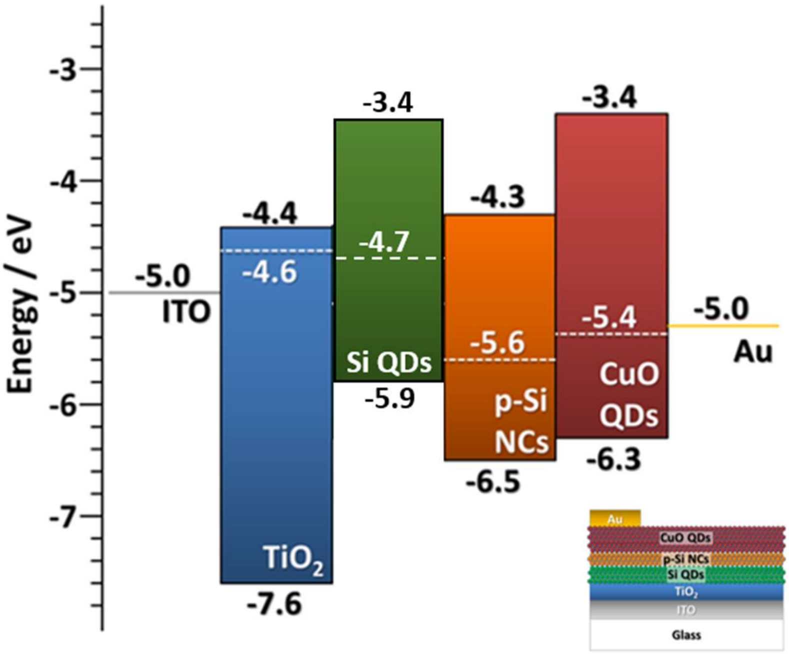

Figure S10. *Non-equilibrated band diagram for the PV device based on Si QDs as active layers and CuO QDs as electron blocking layer. Inset, diagram of the layer structure of the relative device .*

	J_{sc} [µA cm^{-2}]	**V_{oc}** [mV]	**FF [%]**	**η** [% · 10^{-3}]	**R_{series}** [kΩ/cm^2]	**R_{shunt}** [kΩ/cm^2]
Device I (figure 6 Main paper)	9.3 ± 1.5	785 ± 10	87 ± 11	6.3 ± 0.3	2.7 ± 0.6	32 ± 1
Device II (figure S10)	6.4 ± 3.2	779 ± 40	53 ± 6	2.7 ± 1.2	65 ± 5	200 ± 12

Table S10. Relative performance of tested PV cells, the types refer to the diagrams in figure 6 and S10.

[6] V. Svrcek, A. Slaoui and J.-C. Muller, 2004, *J. Appl. Phys.*, **95**, 3158–3163

[7] Velusamy T, Mitra S, Macias-Montero M, Svrcek V and Mariotti D, 2015, *ACS Appl. Mater. Interfaces*, 2015, *7* (51), 28207–28214

[8] Velusamy T, Liguori A, Macias-Montero M, et al. *Plasma Process Polym*. 2017; **14**: e1600224.